Journal of Thermal Analysis and Calorimetry (2020) 139:17–28
https://doi.org/10.1007/s10973-019-08423-1

A new implementation of electrochemical impedance spectroscopy (EIS) and other methods to monitor the progress of hydration of strontium monoaluminate ($SrAl_2O_4$) cement

Dominika Madej[1]

Received: 23 February 2019 / Accepted: 29 May 2019 / Published online: 7 June 2019

Abstract
Electrochemical impedance spectroscopy has been employed to monitor hydration of strontium monoaluminate ($SrAl_2O_4$) cement. Other supported techniques such as X-ray diffraction, Fourier transform infrared spectroscopy, scanning electron microscopy with energy-dispersive X-ray spectroscopy, thermal analysis (DSC–TG–EGA) and microcalorimetry were also used. In the impedance spectrum at 102 day on a 0.5 water/cement ratio paste, a large double depressed low-frequency arc, a single depressed arc at middle-frequency region and a small part of a large depressed arc at high-frequency region were discriminated. It was due to the specific phase composition and crystal phase content in the fully hardened cement paste. Hence, the new electrochemical equivalent model $R_1(C_1(R_2W_1))(C_2(R_3W_2))(C_3(R_4W_3))(C_4(R_5W_4))$ was implemented and fitted to the experimental results of the fully hydrated and hardened SrAH cement paste. Various hydration products including crystalline Sr_3AH_6, and amorphous phases $SrAH_7$ and AH_3-gel were formed at an early age of hydration. At final hydration process, the main reaction products detected are the ones most thermodynamically stable, i.e. crystalline Sr_3AH_6 and $Al(OH)_3$. The heat evolution of $SrAl_2O_4$ cement under different temperatures (20 °C and 40 °C) was examined by isothermal calorimetry. The curing temperature was found to have a visible effect on cement hydration kinetics.

Keywords Strontium monoaluminate ($SrAl_2O_4$) · Electrochemical impedance spectroscopy (EIS) · Equivalent circuit models · Hydration · Microstructure

Introduction

With the recent dynamic quest for developing sustainable ceramics, refractory materials and building materials, it has been found that there is a need for more advanced material characterization techniques that can provide valuable insight into the nature and fundamental behaviour of the new classes of cementitious materials as fast as they are becoming available. These methods can be implemented for understanding and predicting, for example, cement hydration kinetics, microstructure development and long-term performance of various cementitious systems. Examples of these novel techniques that have been recently used for cementitious material characterization include X-ray photoelectron spectroscopy (XPS), nuclear magnetic resonance spectroscopy (NMR), X-ray microtomography and atomic force and lateral force microscopy (AFM and LFM) [1–3] apart from the most commonly used in cement chemistry, such as X-ray diffraction (XRD), Fourier transform infrared spectroscopy (FT-IR) and scanning electron microscopy with energy-dispersive X-ray spectroscopy (SEM–EDS). Recently, AC electrochemical impedance spectroscopy (EIS) has been demonstrated to be a promising technique for tracing hydration feature of different cementitious systems [4–10]. It is well known that, immediately after mixing cement, a gel layer forms on the surfaces of the cement grains. Substantially, morphological changes in microstructure during the cement hydration process occur, mainly due to its transformation from the viscous liquid to the solid state. The cement minerals are replaced by new solid hydration products,

✉ Dominika Madej
dmadej@agh.edu.pl

[1] Department of Ceramics and Refractories, Faculty of Materials Science and Ceramics, AGH University of Science and Technology, al. A. Mickiewicza 30, 30-059 Kraków, Poland

whereas the pore solution acts as a necessary transition zone between the two solid states. Hence, the unique EIS response of hydrating cement paste should be expected at each stage of reaction.

The early stage of the cement paste hydration, where a liquid phase of the saturated cement paste dominates and a significant movement of ions occurs in the pore solution, can be considered as a simple electrochemical system. A typical electrical equivalent circuit of $R_1(C(R_2W))$ type can be used to simulate the experimental results [9], where R_1 denotes the solution resistance, C is related to the double-layer capacitance of the electrodes/electrolyte interface, R_2 stands for charge transfer resistance of the electrodes/electrolyte interface and W considers the Warburg character associated with some diffusional processes at the electrode/paste interface [4, 8, 11]. In a recent study, Madej and Kruk [12] develop a novel electrochemical equivalent model $R_1(CPE(R_2W_1))W_2$ that can better explain phenomena of the early stage hydration process of cementitious compounds. At the mid of the cementing materials hydration process, cement paste hardens, its ion content decreases gradually and the high-frequency arc in the impedance spectrum appears. Hence, the impedance spectrum shows both electrode and bulk features, and the following electrochemical model $R_1(C_1(R_2W_1))(C_2(R_3W_2))$ successfully describes the impedance response of the hardened cement paste [4, 8, 12].

Major progress has also been made to date in the development of novel cement-based systems such as C–A–Z–H, C–Sr–A–Z–H and Sr–A–H (C = CaO, A = Al_2O_3, Sr = SrO, Z = ZrO_2) materials containing mainly calcium/strontium aluminate hydrates [13–23]. Nowadays, cements containing strontium aluminate phases are currently being evaluated for technological applications owing to their unique both physical and chemical properties over other high alumina cements such as calcium aluminate cements (CACs). The applications, such as dense or thermal insulating refractory materials, and the binding materials used for preparing radiation shielding concrete to protect against X-ray and gamma radiation are supposed for strontium aluminate cements [24]. Strontium monoaluminate $SrAl_2O_4$ (SrA; S = SrO, A = Al_2O_3) is an analogue of the well-known calcium monoaluminate $CaAl_2O_4$. According to the calculated binary phase equilibrium diagram of SrO–Al_2O_3 given by Ye et al. [25], the congruent melting point of $SrAl_2O_4$ is determined to be 1960 °C.

This scientific paper aims at providing a new implementation of electrochemical impedance spectroscopy (EIS) method to monitor the hydration of strontium monoaluminate ($SrAl_2O_4$) cement. In this aspect, this study was undertaken to examine more closely the impedance behaviour of special cement paste throughout the hydration process, giving special attention to a novel electrochemical equivalent model.

Materials and methods

Synthesis

The reagent grade chemicals, strontium carbonate (99.00% $SrCO_3$, Merck) and alumina α-Al_2O_3 (99.8% Al_2O_3, Acros Organics), were used as the starting materials. Synthesis of strontium monoaluminate $SrAl_2O_4$ was accomplished in a two-step firing process. An intermediate grinding/mixing stage of calcined mixture was necessary in order to improve its homogeneity. In a first step, raw materials were mixed with the 1:1 molar ratio of SrO and Al_2O_3 oxides, and then the mixture was homogenized for 2 h in a zirconium ball mill and pressed into cylinders having a diameter of 2 cm. All green pellets were calcined at 1300 °C for 10 h. In a second step, solid-state sintering of the pellets made from the calcined powder at 1550 °C for 15 h resulted in a phase $SrAl_2O_4$. The heating rate for both the calcination and sintering was 2 °C min^{-1}.

Cement paste preparation, tests and procedures

The specimen for the impedance measurement was prepared by hand mixing in an ambient atmosphere with water-to-cement ratio (w c^{-1}) of 0.5. The water-to-cement ratio of 0.5 was applied to achieve a viscous suspension without any undesirable sedimentation of neat SrAH cement paste. In a typical experiment, after casting the fresh cement paste, two pieces of stainless steel with smooth surfaces were separated from each other by a spacing between the electrodes being 1.5 cm and immediately immersed in the SrAH cement paste. Each electrode comprised a 2.5-mm-diameter stainless steel rod (approximately 3 cm in length) with the comparable working electrode active area. The sample was cured at 95% humidity conditions. Two-point electrical impedance measurements were obtained on each sample using a Potentiostat/Galvanostat AutoLab PGSTAT302 N frequency response analyser (FRA). The signal amplitude used in the experimental programme was 0.05 V with the impedance measured over the frequency ranges 1 MHz–100 Hz (4-day-hydrated SrAH cement paste), 1 MHz–0.1 Hz (18-day-hydrated SrAH cement paste) and 1 MHz–170 Hz (102-day-hydrated SrAH cement paste) using a logarithmic sweep with 100 frequency points per decade. In order to obtain the equivalent circuits to explain the different possible behaviours of the cement paste after different moist curing periods, EIS experimental data were correlated with data from the simulation EIS Spectrum

Analyser software. Kramers–Kronig relationships (K–K test) were adapted in order to analyse the validity of the experimental impedance results.

Simultaneous thermal analysis [i.e. differential scanning calorimetry (DSC), thermogravimetry (TG) and evolved gas analysis (EGA)], X-ray diffraction (XRD), infrared spectroscopy (IR) and scanning electron microscopy with energy-dispersive spectroscopy (SEM–EDS) were used to trace phase changes in $SrAl_2O_4$–H_2O system as a function of time. SrAH cement paste was made from $SrAl_2O_4$ micro-powder and water (w c^{-1} = 0.5). Paste was hand-mixed for 1 min, then poured into sealed polyethylene bag and cured in a climatic chamber with the relative humidity maintained at 95% and temperature of 20 °C. At time intervals of 4, 18 and 102 days, the samples were immersed in acetone to terminate the hydration and air-dried. The NETZSCH STA 449 F5 Jupiter coupled to QMS 403 D Aëolos apparatus was designed for simultaneous thermal analysis (heating rate of 10 °C min^{-1}, a flow of Ar (50 mL min^{-1}) and α-Al_2O_3 as a standard substance). The Fourier transform infrared spectrometer from Bruker (Vertex 70) was designed to record IR spectra in the 400–4000 cm^{-1} range. KBr pellets method was applied. Nova NanoSEM 200 from FEI Europe Company with EDS analyser from EDAX was used to observe microstructure and to find the chemical composition in micro-areas of cement paste, respectively.

Hydration heat evolution and kinetics of the SrAH cement paste with w c^{-1} = 0.5 were analysed with a TAM air microcalorimeter (TA Instruments) at 20 °C and 40 °C by integrating the continuous heat flow signal during the 72-h hydration process. An admix ampoule which enables cement paste homogenization inside calorimeter was used for this purpose. The apparatus and the measurement procedure were described in detail in Ref. [26].

Results

In situ electrochemical impedance spectroscopy (EIS) experiment

The processes by which SrAH cement paste transforms from a viscous suspension (called a neat cement paste) through a rigid gel/solid into a fully hydrated solid must be understood if the performance of this cement-based materials is to be reliably predicted from EIS measurement. The evolution of SrAH cement paste hydration process by EIS is presented in Figs. 1–8. The time evolution of Nyquist plot for SrAH cement paste is presented in Fig. 1. It can be seen that a semicircle gradually increases along with hydration time increasing. Figure 1 presents changes in parameter R_1 expressed in ohm which corresponds to the

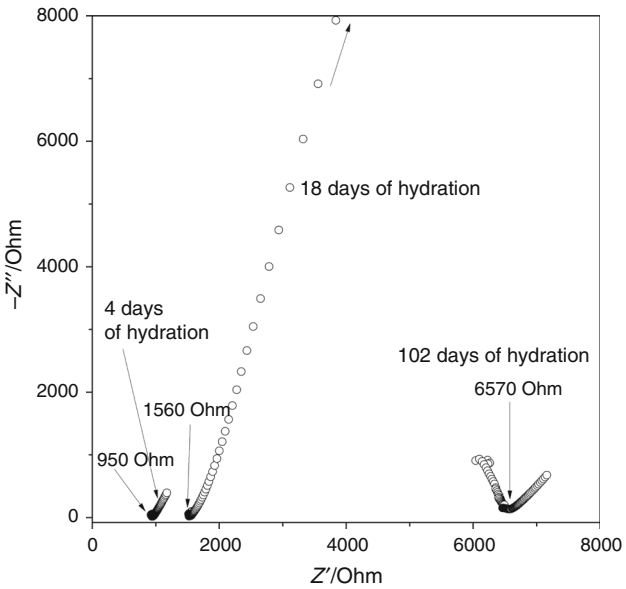

Fig. 1 Time evolution Nyquist plot for the hydrated SrAH cement paste matrix (w c^{-1} = 0.5)

total resistance of samples given by the low-frequency intercept of the impedance with the real axis Z' [27]. This sample exhibited sample resistance of 950, 1560 and 6570 ohm, after 4 days, 18 days and 102 days, respectively. Increase in sample resistance is connected with the formation of solid hydration products since water in the hydrating cement paste can occur mainly in chemically bound (structural water) state.

Concerning the early stage as soon as 4 days (Fig. 2), hydration processes of neat cement paste are proceeded by a dissolution–diffusion–precipitation mechanism. The ionic conditions in the fresh cement paste are unusual because of the extremely high concentration of Sr^{2+}, OH^- and $Al(OH)_4^-$ ions. This system called a fresh cement paste

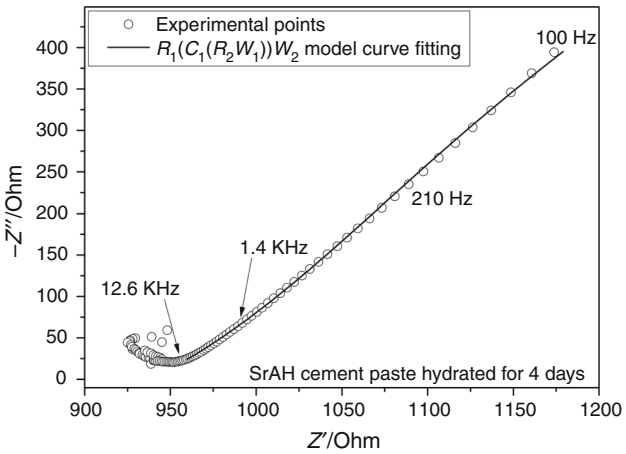

Fig. 2 Nyquist plot and fitted curves of the neat SrAH cement paste (hydration time 4 days; w c^{-1} = 0.5; measurement temperature 20 °C

can be considered as the solution in electrochemical system, and its impedance is rather small due to diffusion of ions in cement paste. At this stage, the effect of the cement paste–electrodes interface (electrode reaction) cannot be ignored. The model is close to the classic electrochemical equivalent model $R_1(C_1(R_2W_1))$ [9]. However, Fig. 2 shows that the new equivalent model $R_1(C_1(R_2W_1))W_2$, presented previously in Ref. 12, is fitted a high degree of SrAH hydration process. This model curve fitting (Figs. 2, 3) exhibits the best match with experimental points than the first one. For wet sample, as the significant movement of the pore solution ions Sr^{2+}, $Al(OH)_4^-$ and OH^-, and "free water" inside neat cement paste occurs, the charge diffusion impedance (Warburg impedance) is significant to be considered in this case. Hence, Warburg impedance in the EIS model $R_1(C_1(R_2W_1))W_2$ is included to consider both the slow ionic diffusion effects at the electrode interface and ionic resistance inside of SrAH cement paste.

At an intermediate stage of the hydration process (18 days), the high-frequency arc was still not defined and only low-frequency arc (Fig. 4) was observed in "rigid gel" SrAH cement paste, suggesting slow hydration. In this case, none of the models proposed in the literature to date give a suitable fit to the EIS data. For example, the classic electrochemical equivalent model $R_1(C_1(R_2W_1))$, the Gu et al.'s model $R_1(C_1(R_2))(C_2(R_3))$ [28] and $R_1(C_1(R_2W_1))(C_2(R_3W_2))$ tested or adopted by Dong et al. [4] were not able to fit to the EIS data. Figure 4 shows that the new equivalent circuit model $R_1(C_1(R_2W_1))(C_2(R_3W_2))W_3$ (Fig. 5) fits perfectly the experimental points. As will be argued below, this spectrum consists of not one, but two semicircles as it has been proposed in Ref. 8. Firstly, it can be associated with both the viscosity change in the SrAH cement paste and paste phase composition change over hydration time. In this respect, as noted previously by Madej and Kruk [12], the ionic transport in cementitious materials with ion–cement hydrates interactions should also be taken into consideration. Hence, Warburg impedance in the EIS model $R_1(C_1(R_2W_1))(C_2(R_3W_2))W_3$ is included to consider both the slow ionic diffusion effects at the electrode interface and ionic resistance inside the "rigid gel" SrAH cement paste. Secondly, the samples can show a different behaviour at low-frequency region due to the effect of electrode geometry or its choice.

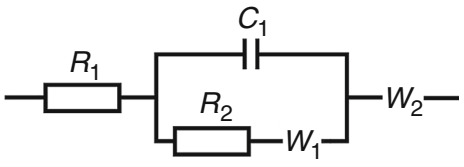

Fig. 3 Equivalent circuit model according to fitted curve presented in Fig. 2. Fitted spectrum $R_1(C_1(R_2W_1))W_2$

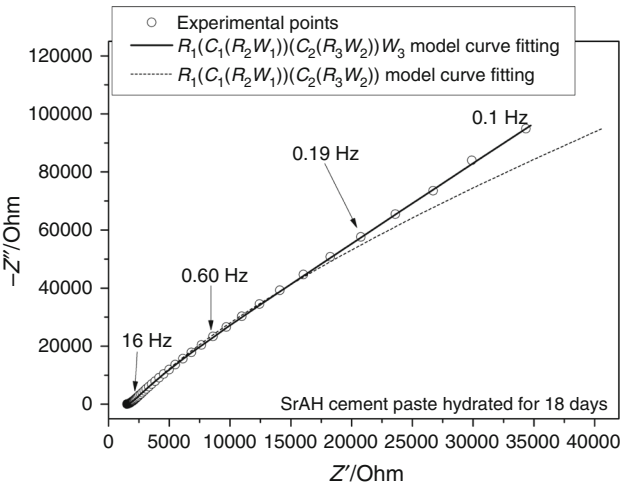

Fig. 4 Nyquist plot and fitted curves of the "rigid gel" SrAH cement paste (hydration time 18 days; w c^{-1} = 0.5; measurement temperature 20 °C

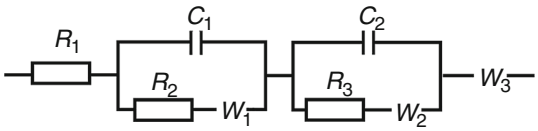

Fig. 5 Equivalent circuit model according to fitted curve presented in Fig. 4. Fitted spectrum $R_1(C_1(R_2W_1))(C_2(R_3W_2))W_3$

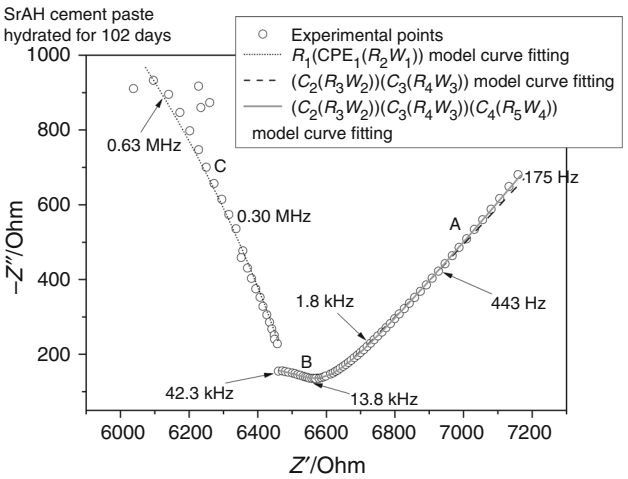

Fig. 6 Nyquist curve and fitted curves of the fully hardened SrAH cement paste (hydration time 102 days; w c^{-1} = 0.5; measurement temperature 20 °C

As expected, the bulk resistance increases with long-term hydration due to the consumption of ions and the formation of hydration product crystals. Impedance spectrum at 102 days on a 0.5 water/cement ratio paste over the frequency range 100 Hz–1 MHz shows both electrode-dominated features ("A") at low frequencies and bulk features ("B", "C") at high frequencies (Fig. 6). At long

times, two bulk arcs can be discriminated which are identified as being due to bulk features "C" and "B" of the sample and appear at higher frequencies. The existence of two partially merged arcs, first within the frequency range ca. 13.8–42.3 kHz and second within the frequency range ca. 73.9 kHz–1 MHz, is a new feature and must be as a direct result of the presence of both C_3AH_6 and $Al(OH)_3$ well-developed crystals as it will be presented as part of SEM results (Fig. 16). Similar to what was done for the SrAH rigid gel (Figs. 4, 5), the experimental arcs in the impedance spectrum at low frequencies (feature A in Figs. 6, 7) were fitted to the circuit $(C_3(R_4W_3))(C_4(R_5W_4))$. This more complex model gives a better fit to the experimental data than the $C_3(R_4W_3)$ (dash line in Fig. 6), and the two sub-elements were added to improve the model results of the electrode arc, since the SrAH cement paste–electrode interface was transformed from the "liquid–solid interface" to the "solid–solid interface". Therefore, the electrochemical model $R_1(CPE_1(R_2W_1))(C_2(R_3W_2))(C_3(R_4W_3))(C_4(R_5W_4))$ (Figs. 6, 7) effectively characterizes EIS response of the "fully hydrated" SrAH cement paste. Taking into consideration the fact that the ions are still able to move on a small scale in the hardened SrAH cement paste, Warburg elements are still included in the impedance arcs (Fig. 6). For the above equivalent circuit models, the impedances of these electrochemical equivalent circuits can be deduced as given in "Appendix"—deduction of the impedance equations for the proposed models.

Furthermore, as can be seen in Bode plot representing modulus of impedance |Z| versus frequency (Fig. 8), there is a very strong dependence of overall impedance module |Z| of the "rigid gel" SrAH cement paste at the low frequencies. In the higher-frequency region, |Z| tends to become constant. This is a typical response for the resistive behaviour and corresponds to the solution resistance of cement slurry or hydrated cement paste structure at early age. The situation changes significantly for the "fully hydrated" SrAH cement paste. A very strong dependence of the impedance module |Z| on the frequency within the range of high frequencies (50 Hz–1 MHz) can be observed in the Bode plot of impedance spectra for the 102-day-hydrated cement paste. It shows that the well-developed solid hydration products response exhibits the frequency-dependent |Z| characteristic.

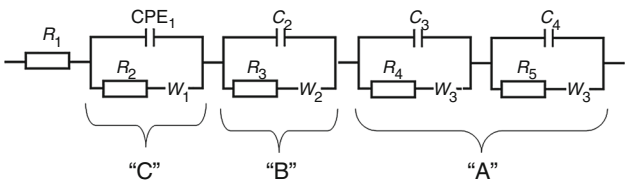

Fig. 7 Equivalent circuit model according to fitted curve presented in Fig. 6. Fitted spectrum $R_1(CPE_1(R_2W_1))(C_2(R_3W_2))(C_3(R_4W_3))(C_4(R_5W_4))$

Kinetics of strontium monoaluminate hydration and detection of its hydration product

The experimental results of isothermal calorimetry, X-ray diffraction (XRD), infrared spectroscopy (IR), simultaneous thermal analysis (DSC–TG–EGA) and scanning electron microscopy with energy-dispersive spectroscopy (SEM–EDS) were applied to analyse the hydration progress of strontium monoaluminate ($SrAl_2O_4$) cement paste prepared with a water-to-cement ratio of 0.5. The relevant results are presented in Figs. 9–16, respectively.

Isothermal calorimetric measurements were taken in order to observe how the temperature affects the strontium monoaluminate cement when mixed with water. The reaction, represented by Eq. 1,

$$3SrA + 12H \rightarrow Sr_3AH_6 + 2AH_3, \quad (1)$$

is accompanied by the release of energy in the form of heat of hydration. It appears to be accelerated by temperature (Figs. 9, 10). When mixed with water at 20 °C, a rapid evolution of heat occurs without any dormant period or induction period of relative inactivity (Fig. 9a). The first conduction calorimetry peak occurring within the first 30 min after mixing of cement and water is due to a combination of the heat of wetting and the heat generated by the cement's hydration (Fig. 9b stage I). The main or 2nd peak (stage II) occurring without any dormant period corresponds to the middle-stage hydration reactions which have strontium aluminate hydrates as the main products. These reactions occur within ca. 1–20 h. The final period called the diffusion-limited reaction period occurs from ca. 25 h of hydration as the hydration product layer around the primary cement particles becomes thicker with time.

The intensity of the initial peak (Fig. 9a initial reaction period) corresponding to the wetting of the cement and the beginning of $SrAl_2O_4$ dissolution increases with an increase in the temperature measurement from 20 to 40 °C (Fig. 9b). The two exothermic stages were more clearly isolated from one another than in the case of the SrAH cement paste measured at 20 °C. The first exothermic stage corresponds to the formation of saturated solution, and the second exothermic part (acceleration and deceleration periods) to the formation of solid hydration products. The induction period (slow reaction period), i.e. a time of minimal hydration activity between the initial hydration reactions upon wetting and the later primary $SrAl_2O_4$ reaction with water to form hydrates, occurs between ca. 5 and 20 h of hydration (Fig. 9a).

Figure 10 shows an integration of the heat evolved over time of hydration, i.e. the total evolved heat. During the

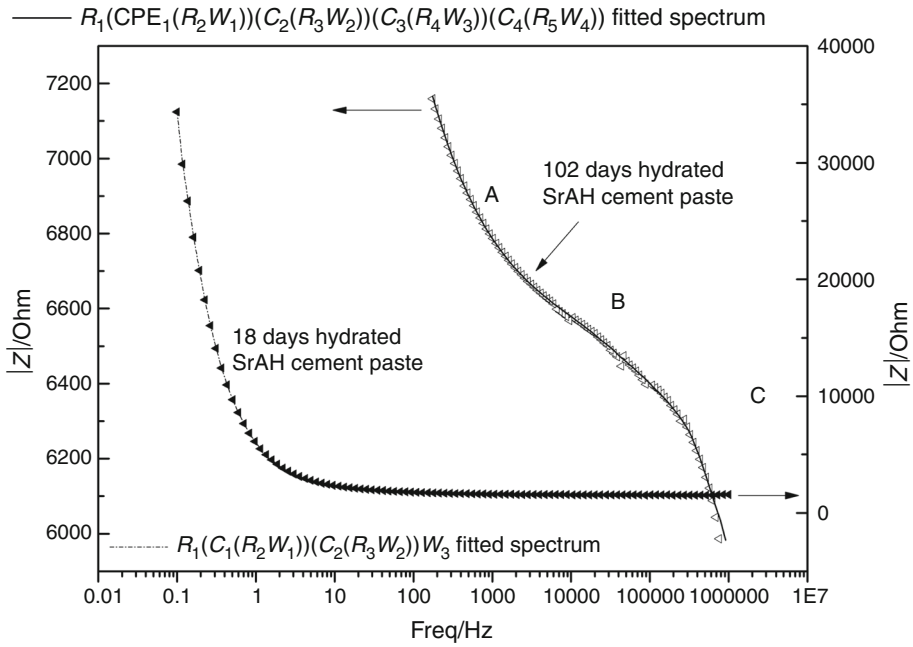

Fig. 8 Bode plots of EIS measurement for SrAH (w c^{-1} = 0.5) at 18-day and 102-day hydration period

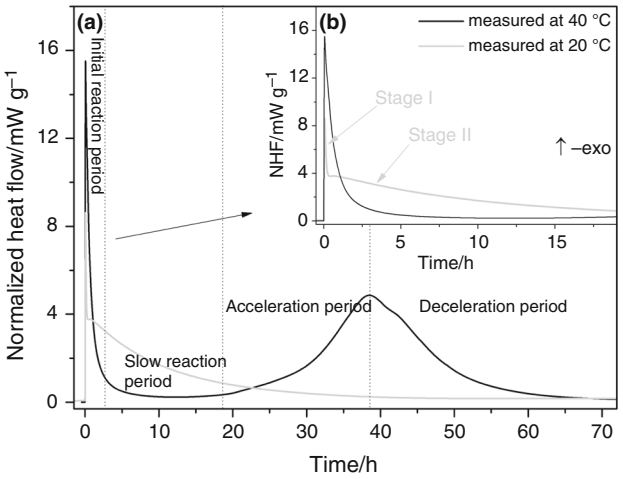

Fig. 9 Heat flow curves of SrAH cement pastes hydrated at 20 °C and 40 °C, normalized to mass of dry powder (with in situ mixing procedure)

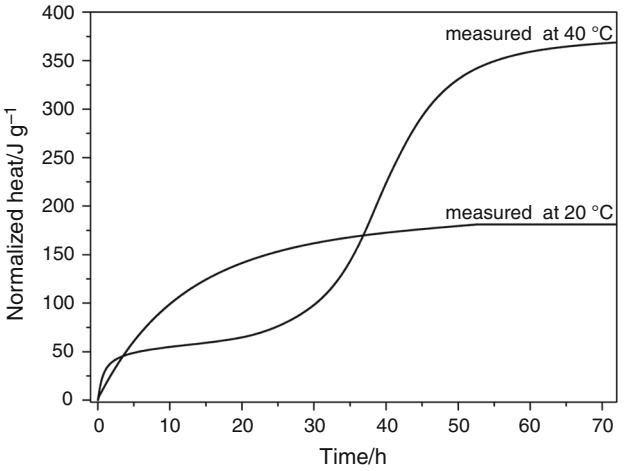

Fig. 10 Cumulative heat release curves versus time for the SrAH cement pastes hydrated at 20 °C and 40 °C for w c^{-1} = 0.5

course of hydration, the cumulative heat evolved due to hydration of $SrAl_2O_4$ cement at 40 °C was higher than from hydrated at 20 °C after 72 h. Here, it is interesting that the hydration process was retarded between ca. 5 and 20 h since a dense Sr–A–H envelope forms around the strontium monoaluminate cement grains within the first few hours after mixing with water.

Cement paste of the synthesized strontium monoaluminate cement, with a water-to-cement (w c^{-1}) ratio of 0.5, was examined by the X-ray diffraction (XRD) method to identify the crystalline hydration products after 4 and 102 days (Fig. 11). The results show an important reduction in intensity of the phase $SrAl_2O_4$ due to its hydration, which leads to the formation of the cubic tri-strontium aluminate hexahydrate phase (Sr_3AH_6) and the high alumina phase (gibbsite γ-AH_3). Newly formed Sr–A–H phases are the typical components observed in hardened strontium monoaluminate cement paste [19]. The sample still contains traces of un-hydrated strontium monoaluminate phase in 102nd day of hydration (Fig. 11c), indicating that the hydration reaction is very slow after ca. 4 days of hydration.

Figure 12 compares the IR spectrum of un-hydrated strontium monoaluminate cement (a.) and SrAH cement

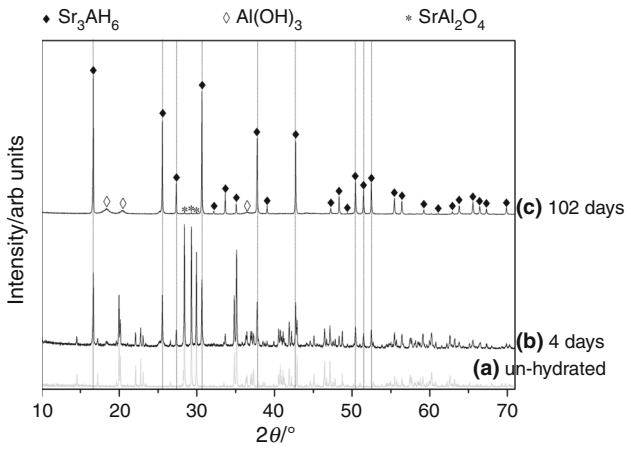

Fig. 11 X-ray diffraction patterns of un-hydrated strontium monoaluminate cement (*a*), SrAH cement paste after 4 days of hydration (*b*), and SrAH cement paste after 102 days of hydration (*c*)

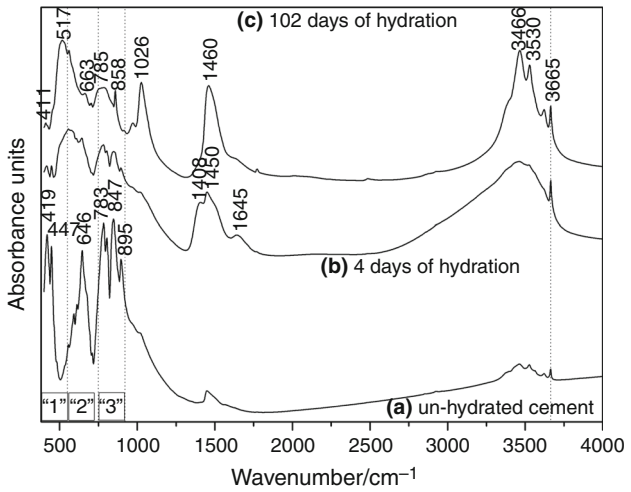

Fig. 12 FT-IR spectrum of un-hydrated strontium monoaluminate cement (*a*), SrAH cement paste after 4 days of hydration (*b*), and SrAH cement paste after 102 days of hydration (*c*)

paste after 4 days (b.) and 102 days (c.) of hydration. The $SrAl_2O_4$ structure contains the rings formed by six corner-sharing AlO_4 tetrahedra and large divalent cations, Sr^{2+} ions, that occupy the interstitial sites to compensate for the charge imbalance [23]. The bands appearing in the regions of 750–920 cm^{-1} ("3") and 550–700 cm^{-1} ("2") belong to antisymmetric and symmetric stretchings of (AlO_4) tetrahedra. The bands related to the doublet of the O–Al–O bending vibration of AlO_4 tetrahedra are located at 447 and 419 cm^{-1} ("1") (Fig. 12a).

The IR spectra (Fig. 12b, c) confirmed the mineralogical composition of the investigated hydrating sample as determined by means of XRD. As a result of the interaction between cement particles and water, the infrared band of the $SrAl_2O_4$ decreased in intensity and the other new bands belonging to hydration products started to appear and increased in intensity upon the hydration time. The IR spectrum of the 102-day paste (Fig. 12c) is practically identical with absorptions assignable to cubic hydrate and aluminium hydroxide. The characteristic infrared bands of Sr_3AH_6 are 3665 cm^{-1} (OH stretching band), 785 cm^{-1} and 517 cm^{-1}. According to Tarte [29], the assignment of the strong band observed at 517 cm^{-1} to the "pure" AlO_6 vibration is evident. This spectrum exhibits a series of well-defined bands observed at 3622, 3530, 3466, 3395, 1026 and 972 cm^{-1}, confirming the attribution of this band to gibbsite $Al(OH)_3$ [30]. In particular, the characteristic strong bands of gibbsite $Al(OH)_3$ are 3530 and 3466 cm^{-1} due to the O–H–O stretching vibration and 1026 cm^{-1} due to the –OH bending vibration. The mid-IR spectrum of the fully hydrated SrAH cement paste (Fig. 12c) clearly shows strong v_2 CO_3^{2-} and v_4 CO_3^{2-} modes around 858 cm^{-1} and 663 cm^{-1}, respectively. The band at 1460 cm^{-1} was generated by the antisymmetric stretching vibration (v_3) of carbonate CO_3^{2-} anion.

The IR spectrum of the partly hydrated cement paste (Fig. 12b) contains absorption bands of both un-hydrated $SrAl_2O_4$ and strontium aluminate hydrates. The sharp band at 3665 cm^{-1} can be taken as characteristic of OH group vibrations in hydrated strontium aluminate of cubic type. The formation of Sr_3AH_6 hydrate in this sample was also confirmed by XRD. Moreover, a very broadband in the region between 3100 and 3600 cm^{-1} may indicate the presence of hydrated strontium aluminate other than the cubic one and the alumina gel (AH_3 gel). Similarly, a weak band at 1645 cm^{-1} corresponding to H_2O deformation mode supported the evidence for the presence of hydrated strontium aluminate other than the cubic type. Additionally, the absorption band at 1408 cm^{-1} is characteristic of AH_3 gel [19].

In the present paper, thermogravimetry was used for studying the hydration of $SrAl_2O_4$ cement; hence, the hydration reaction between the mixing water and cement can be reversed when the hardened cement paste is subjected to high temperatures. The SrAH cement paste after 4 and 102 days of hydration at 20 °C was analysed by simultaneous DSC–TG–EGA analysis, and the related thermal curves received from the hydrated cement paste are presented in Fig. 13a, b. The degree of hydration was determined based on the thermogravimetric analysis (TG) results after specific hydration time intervals. It was stated that, as the duration of SrAH cement paste curing increases, the content of hydration products also increases because the mass loss at 800 °C increases from 20.23 to 26.96% (Fig. 13a, b).

The H_2O–EGA curve of the 4-day-cured SrAH sample (Fig. 13a) records two stages of volatile product evolution, with the peaks at ca. 100 °C and 270 °C, by hydration

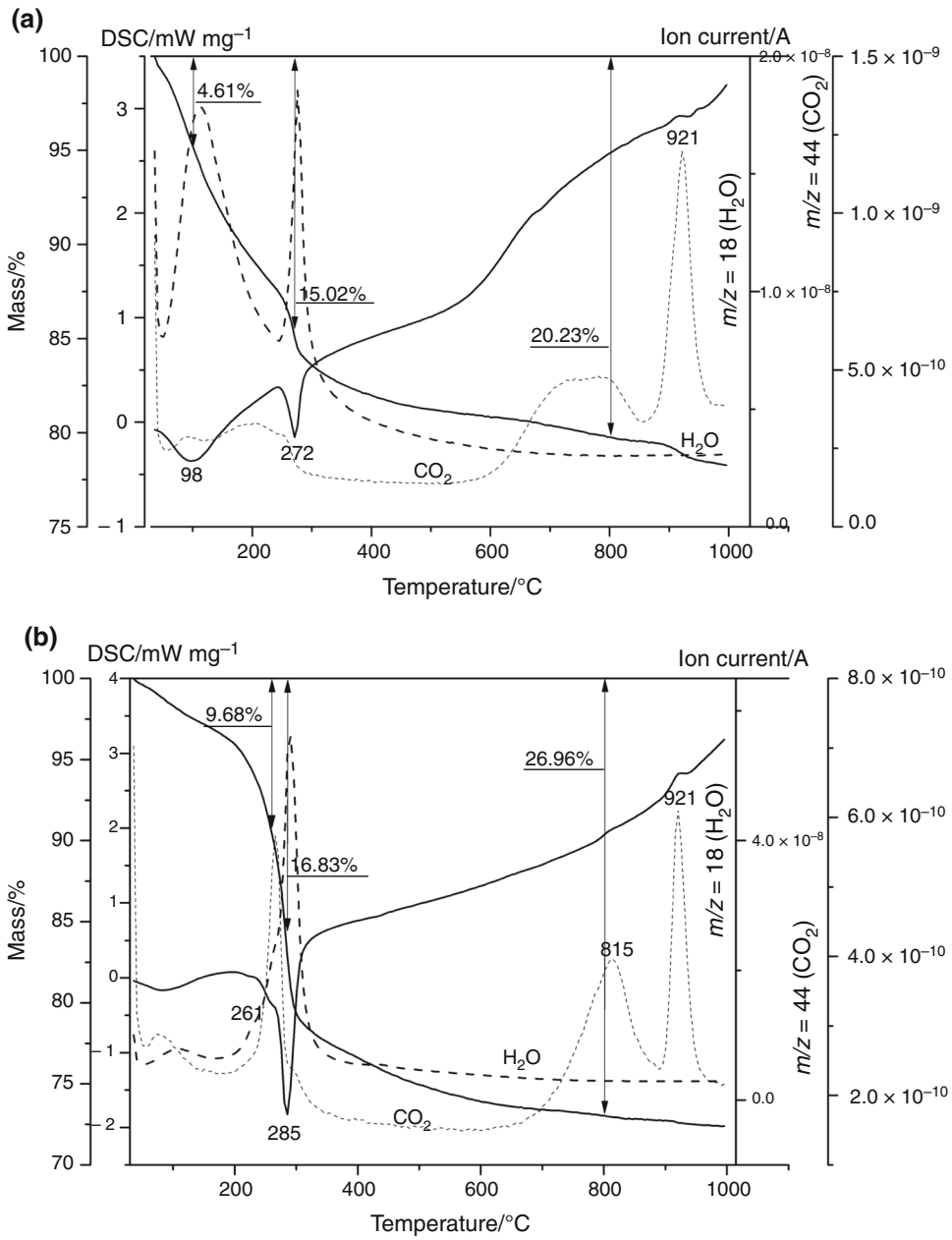

Fig. 13 Result of the simultaneous thermal analysis DSC–TG–EGA of the SrAH cement paste after 4 days of hydration (**a**) and SrAH cement paste after 102 days of hydration (**b**)

products, and these are also indicated by two endothermic effects. It can be noted that the first endothermic peak at ca. 100 °C represents two overlapping dehydration of both amorphous $SrAH_7$ and AH_3 gel. The second endothermic effect at 272 °C corresponds to decomposition of the cubic tri-strontium aluminate hexahydrate (Sr_3AH_6).

The second strong endothermic peak due to the decomposition of Sr_3AH_6 is sharp and shifts to higher temperature at increased hydration time (Fig. 13b). The second stable phase in the SrAH hydrated cement paste at 102 day of hydration is gibbsite γ-$Al(OH)_3$. Its presence is indicated by a small inflection on the low-temperature side of the principal endotherm of the cubic hydrate at ca. 261 °C. It may be also seen that during the periods of hydration the SrAH cement paste carbonated which was determined by analysing the CO_2–EGA curves of both samples (Fig. 13a, b). When Sr_3AH_6 hydrate comes in contact with atmospheric CO_2, a carbonation reaction occurs according to Eq. 2.

$$Sr_3AH_6 + 3CO_2 + xH_2O \rightarrow 3SrCO_3 + Al_2O_3 \cdot yH_2O + (6 + x - y)H_2O. \quad (2)$$

It should be noted that a small quantity of minor phases can be undetectable by XRD analysis, especially in this case of diffraction patterns with wide reflections of unhydrated phase and hydration products. However, $SrCO_3$ in relatively minor amount appears slightly above background at ca. $2\theta = 25.232^\circ$ (JCPDS Card No. 01-074-1491) in the X-ray diffraction pattern of 4-day-hydrated sample (Fig. 11b). It is worth mentioning that the presence of $SrCO_3$ is dependent on the sample preparation conditions. As presented in the "Cement paste preparation, tests and procedures" section, cement paste sample was soaked or ground with an excess of acetone and inevitably exposed to CO_2 from air.

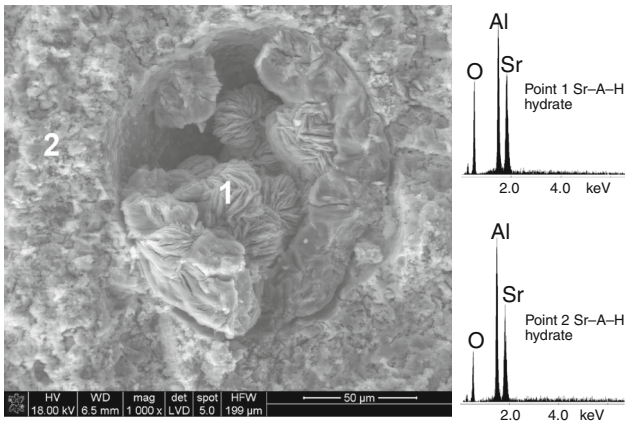

Fig. 14 SEM image of the fracture surface of 11-day-hydrated strontium aluminate cement paste. EDS analysis: 1, 2—strontium aluminate hydrates other than the cubic type

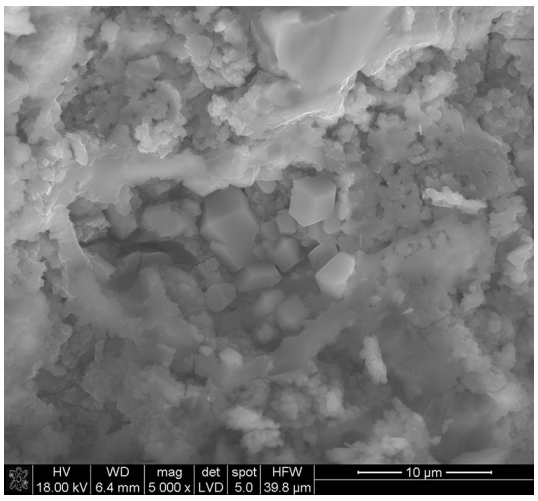

Fig. 15 SEM image of the fracture surface of 11-day-hydrated strontium aluminate cement paste with some Sr_3AH_6 crystals

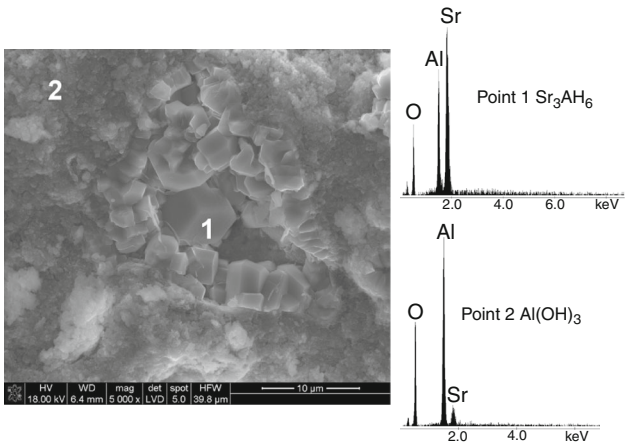

Fig. 16 SEM image of the fracture surface of 102-day-hydrated strontium aluminate cement paste. EDS analysis: 1—cubic tristrontium aluminate hexahydrate phase (Sr_3AH_6), 2—aluminium hydroxide ($Al(OH)_3$)

The microstructure of hydration products of the strontium monoaluminate cement paste was examined by SEM–EDS at different hydration times (Figs. 14–16). These SEM micrographs show that the hydration time gave morphologically different hydration products. The flower-like crystals of Sr–A–H (Fig. 14—point 1) and spongy-type Sr–A–H hydrates (Fig. 14—point 2) were the major hydration products, and they were formed at the age of 11 days of hydration at 20 °C. Some cubic crystals of Sr_3AH_6 are also visible in the SEM micrograph, along with crystals of other Sr–A–H hydration products (Fig. 15). At late hydration period (102 days), the cubic crystals of Sr_3AH_6 (point 1) and $Al(OH)_3$ (point 2) are dominating products present on the fractured surface of the SrAH cement paste (Fig. 16).

Conclusions

This paper deals with the in situ electrochemical impedance characterization of strontium monoaluminate ($SrAl_2O_4$) cement paste to examine early stage of hydration and the long-term hydration characteristics. Various supported techniques (XRD, FT-IR, SEM–EDS, DSC–TG–EGA, isothermal microcalorimetry) were also used to monitor the solid phase changes occurring during hydration process. The major conclusions are as follows:

1. The work has opened up new area for the direct application of impedance spectroscopy techniques, namely as a method for control of $SrAl_2O_4$ hydration features.

2. Equivalent circuit models and impedance formulas $R_1(C_1(R_2W_1))W_2$ and $R_1(C_1(R_2W_1))(C_2(R_3W_2))W_3$ for the SrAH neat cement paste and SrAH rigid gel were proposed, respectively. The results of this modelling are adequate for the early hydration characteristics of $SrAl_2O_4$.
3. Impedance spectra of the fully hydrated strontium monoaluminate cement paste showed a large double depressed low-frequency arc, a single depressed arc at middle-frequency region and a small part of a large depressed arc at high-frequency region. It was due to the specific phase composition and crystal phase content (Sr_3AH_6 and $Al(OH)_3$) of the fully hardened cement paste. Thus, a new electrochemical equivalent circuit model $R_1(CPE_1(R_2W_1))(C_2(R_3W_2))(C_3(R_4W_3))(C_4(R_5W_4))$ was established and used for the long-term age of $SrAl_2O_4$ cement.
4. From the XRD, FT-IR, DSC–TG–EGA and SEM–EDS measurements, it was found that the crystalline and thermodynamically stable Sr_3AH_6 and $Al(OH)_3$ hydration products were formed in a fully hydrated $SrAl_2O_4$ cement paste, while amorphous $SrAH_7$ and AH_3 gel together with crystalline Sr_3AH_6 were formed at an early and middle ages of hydration.
5. From the isothermal calorimetry tests at 20 °C and 40 °C, it was found that the curing temperature was found to have a visible effect on $SrAl_2O_4$ cement hydration kinetics.

Acknowledgements This project was financed by the National Science Centre, Poland, project number 2017/26/D/ST8/00012.

Compliance with ethical standards

Conflict of interest The authors declare that they have no conflict of interest.

Appendix

Deduction of the impedance equations for the proposed models:

Repeated Fig. 3

$$Z = R_1 + \frac{R_2 + W_1}{1 + (R_2 + W_1)j\omega C_1} + W_2$$

$$Z = R_1 + \frac{R_2 + \sigma_1\omega_1^{-\frac{1}{2}}(1-j)}{1 + \left(R_2 + \sigma_1\omega_1^{-\frac{1}{2}}(1-j)\right)j\omega C_1} + \sigma_2\omega_3^{-\frac{1}{2}}(1-j),$$

where R_1—the resistance of the pore solution of the "neat" SrAH cement paste, C_1—the double-layer capacitance at the electrodes/"neat" SrAH cement paste interface, R_2—the charge transfer resistance at the electrodes/"neat" SrAH cement paste interface, W_1—Warburg impedance caused by the ion diffusion procedure on the surface of the electrodes, $R_2 + W_1$—the impedance of the Faraday's procedure that occurs on the surface of the electrodes, and W_2—Warburg impedance included to consider the ionic conductivity and other diffusion processes inside the "neat" SrAH cement paste.

Repeated Fig. 5

$$Z = R_1 + \frac{R_2 + W_1}{1 + (R_2 + W_1)j\omega C_1} + \frac{R_3 + W_2}{1 + (R_3 + W_2)j\omega C_2} + W_3$$

$$Z = R_1 + \frac{R_2 + \sigma_1\omega_1^{-\frac{1}{2}}(1-j)}{1 + \left(R_2 + \sigma_1\omega_1^{-\frac{1}{2}}(1-j)\right)j\omega C_1} + \frac{R_3 + \sigma_1\omega_1^{-\frac{1}{2}}(1-j)}{1 + \left(R_3 + \sigma_2\omega_2^{-\frac{1}{2}}(1-j)\right)j\omega C_2} + \sigma_3\omega_3^{-\frac{1}{2}}(1-j),$$

where R_1—the resistance of the pore solution of the "rigid gel" SrAH cement paste, C_1—the capacitance of the "rigid gel" SrAH cement paste, C_2—the double-layer capacitance at the electrode/"rigid gel" SrAH cement paste interface, R_2—the resistance caused by the charge transfer procedure through the "rigid gel" SrAH cement paste, R_3—the charge transfer resistance at the electrodes/"rigid gel" SrAH cement paste interface, $R_2 + W_1$—the impedance of the Faraday's procedure that occurs inside the "rigid gel" SrAH cement paste, $R_3 + W_2$—the impedance of the Faraday's procedure that occurs on the surface of the electrodes, W_1—Warburg resistance caused by the ion diffusion procedure inside the "rigid gel" SrAH cement paste, W_2—Warburg resistance caused by the ion diffusion procedure on the surface of the electrodes, and W_3—

Warburg impedance included to consider other diffusion processes.

Repeated Fig. 7

$$Z = R_1 + \frac{R_2 + \sigma_1\omega_1^{-\frac{1}{2}}(1-j)}{1 + \left(R_2 + \sigma_1\omega_1^{-\frac{1}{2}}(1-j)\right)j\omega C_1} + \frac{R_3 + \sigma_2\omega_2^{-\frac{1}{2}}(1-j)}{1 + \left(R_3 + \sigma_2\omega_2^{-\frac{1}{2}}(1-j)\right)j\omega C_2} + \frac{R_4 + \sigma_1\omega_1^{-\frac{1}{2}}(1-j)}{1 + \left(R_4 + \sigma_3\omega_3^{-\frac{1}{2}}(1-j)\right)j\omega C_3} + \frac{R_5 + \sigma_5\omega_5^{-\frac{1}{2}}(1-j)}{1 + \left(R_5 + \sigma_4\omega_5^{-\frac{1}{2}}(1-j)\right)j\omega C_4},$$

where R_1—the resistance of the "fully hydrated" SrAH cement paste, CPE_1—the bulk capacitance of the phase 1, C_2—the bulk capacitance of the phase 2, C_3—the double-layer capacitance between the hydration products, C_4—the double-layer capacitance at the electrode/the "fully hydrated" SrAH cement paste interface, R_2—the resistance caused by the charge transfer procedure through the phase 1 of the SrAH cement paste, R_3—the resistance caused by the charge transfer procedure through the phase 2 of the SrAH cement paste, R_4—the resistance caused by the ion transfer procedure inside the fully hydrated SrAH cement paste, R_5—the resistance caused by the charge transfer procedure on the surface of the electrodes, W_1, W_2—Warburg resistance caused by the ion diffusion procedure inside the fully hydrated SrAH cement paste, and W_3, W_4—Warburg resistance caused by the ion diffusion procedure on the surface of the electrodes and other ionic diffusion processes.

References

1. Khoshnazar R, Shao Y. Characterization of carbonation-cured cement paste using X-ray photoelectron spectroscopy. Constr Build Mater. 2018;168:598–605.
2. Kupwade-Patil K, Palkovic SD, Bumajdad A, Soriano C, Büyüköztürk O. Use of silica fume and natural volcanic ash as a replacement to Portland cement: micro and pore structural investigation using NMR, XRD, FTIR and X-ray microtomography. Constr Build Mater. 2018;158:574–90.
3. Peled A, Castro J, Weiss WJ. Atomic force and lateral force microscopy (AFM and LFM) examinations of cement and cement hydration products. Cem Concr Compos. 2013;36:48–55.
4. Dong B, Zhang J, Liu Y, Fang G, Ding Z, Xing F. Tracing hydration feature of aluminophosphate cementitious materials by means of electrochemical impedance method. Constr Build Mater. 2016;113:997–1006.
5. McCarter WJ. The a.c. impedance response of concrete during early hydration. J Mater Sci. 1996;31:6285–92.
6. Dotelli G, Mari CM. The evolution of cement paste hydration process by impedance spectroscopy. Mater Sci Eng, A. 2001;303:54–9.
7. Kim Y-M, Lee J-H, Hong S-H. Study of alinite cement hydration by impedance spectroscopy. Cem Concr Res. 2003;33:299–304.
8. Scuderi CA, Mason TO, Jennings HM. Impedance spectra of hydrating cement pastes. J Mater Sci. 1991;26:349–53.
9. Husain A, Kupwade-Patil K, Al-Aibani AF, Abdulsalam MF. In situ electrochemical impedance characterization of cement paste with volcanic ash to examine early stage of hydration. Constr Build Mater. 2017;133:107–17.
10. Kim HC, Kim SY. Electrical properties of cement paste obtained from impedance spectroscopy. J Mater Sci. 1995;30:3768–72.
11. Song G. Equivalent circuit model for AC electrochemical impedance spectroscopy of concrete. Cem Concr Res. 2000;30:1723–30.
12. Madej D, Kruk A. Tracing the early and long-term hydration of fast setting cementitious material ($Ca_7ZrAl_6O_{18}$) and calcium aluminate cement (CAC) pastes by means of electrochemical impedance spectroscopy and other methods. Constr Build Mater. 2018;164:94–102.
13. Madej D. Hydration, carbonation and thermal stability of hydrates in $Ca_{7-x}Sr_xZrAl_6O_{18}$ cement. J Therm Anal Calorim. 2018;131:2411–20.
14. Madej D. Synthesis and hydraulic activity of novel Sr^{2+}-doped $Ca_7ZrAl_6O_{18}$ cement at 50°C. Thermochim Acta. 2018;661:98–105.
15. Madej D. Synthesis, formation mechanism and hydraulic activity of novel composite cements belonging to the system CaO–Al_2O_3–ZrO_2. J Therm Anal Calorim. 2017;130:1913–24.
16. Madej D, Szczerba J. Study of the hydration of calcium zirconium aluminate ($Ca_7ZrAl_6O_{18}$) blended with reactive alumina by calorimetry, thermogravimetry and other methods. J Therm Anal Calorim. 2015;121:579–88.
17. Madej D, Szczerba J, Nocuń-Wczelik W, Gajerski R. Hydration of $Ca_7ZrAl_6O_{18}$ phase. Ceram Int. 2012;38:3821–7.
18. Madej D, Szczerba J, Nocuń-Wczelik W, Gajerski R, Hodur K. Studies on thermal dehydration of the hydrated $Ca_7ZrA_{l6}O_{18}$ at different water-solid ratios cured at 60 °C. Thermochim Acta. 2013;569:55–60.
19. Ptáček P, Šoukal F, Opravil T, Bartoníčková E, Zmrzlý M, Novotný R. Synthesis, hydration and thermal stability of hydrates in strontium-aluminate cement. Ceram Int. 2014;40:9971–9.
20. Fukuda K, Fukushima K. Crystal structure of hexagonal $SrAl_2O_4$ at 1073 K. J Solid State Chem. 2005;178:2709–14.
21. Pöllmann H, Stöber S, Mohr P, Kaden R. In: Fentiman ChH, Mangabhai R, Scrivener KL, editors. Synthesis and crystal chemistry of strontium aluminates, calcium aluminates: proceedings of the international conference, IHS BRE Press, Garston; 2014. pp. 89–98.
22. Pöllmann H, Kaden R. In: Fentiman ChH, Mangabhai R, Scrivener KL, editors. Mono- (strontium-, calcium-) aluminate based cements, calcium aluminates: proceedings of the international conference, IHS BRE Press, Garston; 2014. pp. 99–108.
23. Prodjosantoso AK, Kennedy BJ. Synthesis and evolution of the crystalline phases in $Ca_{1-x}Sr_xAl_2O_4$. J Solid State Chem. 2002;168:229–36.
24. Ptáček P. In: Ptacek P, editor. Applications of strontium aluminate cements, strontium aluminate—cement fundamentals, manufacturing, hydration, setting behaviour and applications. London: IntechOpen; 2014. p. 141–85.
25. Ye X, Zhuang W, Wang JF, Yuan W, Qiao Z. Thermodynamic description of SrO–Al_2O_3 system and comparison with similar systems. J Phase Equilib Diff. 2007;28:362–8.
26. Madej D, Ortmann Ch, Szczerba J, Jacewicz M. Calorimetry and other methods in the studies of reactive magnesia-

hydratable alumina-microsilica hydrating mixtures. J Therm Anal Calorim. 2016;126:1133–42.
27. Macphee DE, Sinclair DC, Cormack SL. Development of an equivalent circuit model for cement pastes from microstructural considerations. J Am Ceram Soc. 1997;80:2876–84.
28. Gu P, Xie P, Beaudoin JJ. Microstructural characterization of the transition zone in cement systems by means of A.C. impedance spectroscopy. Cem Concr Res. 1993;23:581–91.
29. Tarte P. Infra-red spectra of inorganic aluminates and characteristic vibrational frequencies of AlO_4 tetrahedra and AlO_6 octahedra. Spectrochim Acta A Mol Spectrosc. 1967;23:2127–43.
30. Fernández-Carrasco L, Torrens-Martín D, Morales LM, Martínez-Ramírez S. Infrared spectroscopy in the analysis of building and construction materials. In: Prof. Theophanides T, editor. Infrared spectroscopy—materials science, engineering and technology, ISBN: 978-953-51-0537-4, InTech; 2012. https://doi.org/10.5772/36186. http://www.intechopen.com/books/infrared-spectroscopy-materials-science-engineering-and-technology/infrared-spectroscopy-of-cementitious-materials.